Article:
Mason, A.J.W., Friskney, A.A., Haigh, L.T. et al. (2025) Structural and thermal effects of Hf4+ substitution in CaZr1-xHfxTi2O7 zirconolite. Ceramics International, 51 (27, Part A). pp. 52074-52080. ISSN: 0272-8842

https://doi.org/10.1016/j.ceramint.2025.08.415

Structural and Thermal Effects of Hf^{4+} Substitution in $CaZr_{1-x}Hf_xTi_2O_7$ Zirconolite

Alex J. W. Mason[1], Aidan A. Friskney[1], Latham T. Haigh[1], Maciej Myszczynski[2], Ismail Aldean[1], Alexander B. Harvey-Reid[1], Martin C. Stennett[1] and Lewis R. Blackburn[1]*

[1] Immobilisation Science Laboratory, School of Chemical, Materials and Biological Engineering, University of Sheffield, UK
[2] The Henry Royce Institute, Royce Discovery Centre, Harry Brearley Building, University of Sheffield, UK

***Corresponding author**: lewis.blackburn@sheffield.ac.uk

Abstract

There is a requirement to further understand the structural and thermal properties of candidate Pu wasteform materials, and moreover gain a better understanding of composition-driven variation in these properties as they can impact disposability. Zirconolite ($CaZrTi_2O_7$) phases are a candidate wasteform system to immobilise Pu at scale and therefore it is necessary to understand (as far as possible) the isolated influence of cation substitution on specific lattice sites. $CaZr_{1-x}Hf_xTi_2O_7$ is a model system for understanding the microstructural effects of Hf^{4+} substitution and underpin its viability as a neutron absorbing additive that could feasibly be co-immobilised with Pu. Hf^{4+} was capable of wholly substituting for Zr^{4+} at low-to-moderate concentration (i.e. $x \leq 0.60$) after which some minor Hf-phase segregation was observed. Powder X-ray diffraction, Rietveld analysis and Raman spectroscopy were consistent with Hf^{4+} substituting in the Zr^{4+} site and confirmed no additional zirconolite polytypes were formed in addition to 2M. Hf L_3-edge EXAFS analysis was consistent with Hf^{4+} occupying the 7-fold Zr^{4+} site in the zirconolite-2M structure consistent with the targeted substitution scheme. The thermal diffusivity and thermal conductivity of the zirconolite ceramics was generally observed to increase with elevated Hf^{4+} content although no clear compositional trends were identified.

1 Introduction

Plutonium lifecycle is a key aspect of the Nuclear Decommissioning Authority (NDA) research strategy, which outlines a requirement to place all Pu currently held under UK civil safeguards 'beyond reach' [1]. As of 2025, immobilisation within a ceramic wasteform prior to geological disposal is the favoured disposition route and, as such, there are ongoing efforts to underpin a preferred immobilisation technology and develop the current understanding of the mechanical, structural and thermal properties of potential host matrices that could feasibly incorporate Pu at moderate concentration (ca. 20 wt. %). Zirconolite ($CaZrTi_2O_7$) is a candidate ceramic phase that has been identified as a potentially feasible wasteform for the immobilization of separated Pu, and there has been a notable body of published literature aiming to further understand its chemistry with respect to actinide incorporation, either using Pu or relevant surrogates (Ce, U, Th) and additives that will require co-immobilisation with a view to satisfy disposal criteria, namely neutron absorbing additives [2]. When considering geological disposability of radioactive waste, heat generation, radiological risk and the potential for a criticality event to occur must all be considered. As criticality can occur in both ^{239}Pu and the ^{235}U daughter

product there is a requirement for waste packages containing immobilised Pu to co-immobilise a suitable neutron absorber. In order to develop a robust safety case for the geological disposal of ceramic products containing Pu in the immobilised form, it is necessary to demonstrate confidence in the solid solution behaviour of neutron absorbing additives within the host wasteform structure. An improved understanding of doping limits and site substitution constraints will better inform ceramic compositions that can be formulated with Pu without leading to the formation of deleterious secondary phases containing segregated Pu. A recent review highlighted Hf^{4+} as a potential neutron absorbing additive in zirconolite [3] and indeed several examples of successful Hf^{4+} incorporation within this phase have been reported in the wider literature. Vance et al. reported the successful substitution of Hf^{4+} for Zr^{4+} at 50 mol. % and 100 mol. % when fabricated by a solid-state route, i.e. $CaZr_{0.5}Hf_{0.5}Ti_2O_7$ and $CaHfTi_2O_7$ [4] and the synthesis of phase pure $CaHfTi_2O_7$ 'hafnolite' was also reported by Putnam et al. [5]. Begg et al. reported a series of PuO_2-doped zirconolite materials under a range of processing atmospheres to favour either Pu^{3+} or Pu^{4+} [6]. When targeting B-site substitution i.e. $CaHf_{0.9}Pu_{0.1}Ti_2O_7$ a sample of 98% phase reported purity in air, with Pu^{4+} maintained; A-site substitution, targeting Pu^{3+} in $Ca_{0.8}Pu_{0.2}HfTi_{1.8}Al_{0.2}O_7$ and Pu^{4+} in $Ca_{0.8}Pu_{0.2}HfTi_{1.6}Al_{0.4}O_7$ produced 96% and 94% phase purity, respectively, when sintered in air with 100% Pu^{4+} valence for both materials measured by X-ray absorption spectroscopy; these data indicate that zirconolite is capable of self-charge balancing in the absence of charge modifying additives. Zhang et al. attempted the synthesis of the $CaZr_{1-x}Hf_xTi_2O_7$ solid solution by combustion synthesis followed by quick pressing, however despite low reported Hf leach rates ($CaZr_{0.4}Hf_{0.6}Ti_2O_7$ at 90 °C via MCC-1 method in deionised water: 1.11×10^{-8} $g \cdot m^{-2} \cdot d^{-1}$ normalised after 42 d) a moderate perovskite yield was reported throughout the sample matrix [7]. Further syntheses of doped $CaHfTi_2O_7$ ceramics and glass-ceramics have been reported in the work of Caurant et al. [8,9]. As Hf^{4+} is considered a candidate neutron absorbing additive, the aim of the present work is to further underpin the incorporation behaviour of Hf^{4+} within the zirconolite phase, by careful examination of diffraction, microscopy and spectroscopy behaviour between the two end-member compounds $CaZrTi_2O_7$ and $CaHfTi_2O_7$.

2 Experimental Methodology

The $CaZr_{1-x}Hf_xTi_2O_7$ solid solution (where x = 0 – 1.00, Δx = 0.10) was fabricated by a solid-state reaction between component oxides $CaTiO_3$, ZrO_2, HfO_2 and TiO_2 (Merck, 99.9% trace metals basis). Precursors were calcined at 800 °C overnight prior to weighing in the required proportions and added to a Y-stabilised ZrO_2-lined milling jar, with ZrO_2 milling media and isopropanol. Each sample was homogenised by planetary ball milling at 400 rpm for a period of 20 min, with the direction changed at each 5 min interval. The powder slurry was discharged and dried at 80 °C to evaporate excess solvent and sieved through a 1 mm mesh to separate the milling media. Approximately 1 g of each composition was pressed into the walls of a stainless-steel die under a uniaxial force of 3 t and pellets were sintered in air at 1400 °C, with a dwell period at maximum temperature held for 24 h and programmed heating/cooling rates of 5 °C/min. Powder X-ray diffraction data was collected using a Bruker D2 Phaser (Cu Kα, λ = 1.5406 Å) fitted with a Lynxeye position sensitive detector and Ni filter, over the range

10° ≤ 2θ ≤ 70° with a scan rate of 0.02° s^{-1} and 1 s per step. Peak matching and indexing was achieved using the PDF2+ database. Each diffraction profile was analysed using the Rietveld method to extract the lattice parameters of the zirconolite phase using the Bruker TOPAS software package. The microstructure and bulk composition of each pellet was analysed using a Hitachi TM3030 microscope operating at 15 kV accelerating voltage with an approximate working distance of 8 mm. Prior to analysis each pellet was mounted in cold-setting epoxy resin and polished to a 1 μm surface finish and coated with a thin layer of conducting carbon. The microscope was fitted with a Bruker Quantax system for elemental dispersive X-ray spectrometry (EDS) analysis. X-ray absorption spectroscopy (XAS) data were collected at the Hf L_3-edge at Diamond Light Source Beamline B18 using a transmission configuration. Data were collected for compositions x = 0.10, 0.50 and 1.00, representative of material with the nominal compositions corresponding to $CaZr_{0.90}Hf_{0.10}Ti_2O_7$, $CaZr_{0.50}Hf_{0.50}Ti_2O_7$ and $CaHfTi_2O_7$, respectively. The Demeter software package was used to normalise and merge multiple scans into one dataset, with the EXAFS region used to model single scattering paths generated by FEFF for the zirconolite-2M structural model (C2/c). Raman spectra were also collected on samples of $CaZrTi_2O_7$, $CaZr_{0.5}Hf_{0.5}Ti_2O_7$ and $CaHfTi_2O_7$ using a Renishaw InVia Raman microscope equipped with a 2400 mm^{-1} grating. Samples were excited using a 514.5 nm Ar laser at 5 mW power output, scanning for 45 seconds at three points on the sample surface. Data were averaged and smoothed using a Savitsky Golay filter followed by Asymmetric Least Squares background subtraction determined through sensitivity analysis of the 780 cm^{-1} spectral line position and intensity ($\lambda = 1 \times 10^6$, p = 0.004). Laser Flash Analysis (LFA) was performed using a Netzsch LFA 467 Hyper Flash to determine thermal diffusivity and specific heat capacity at 30, 100, 200, 300, 400 and 500 °C. LFA data were collected on 13 mm disks polished to 1 μm surface finish, with material density established by He pycnometry and the Archimedes method.

3 Results and Discussion

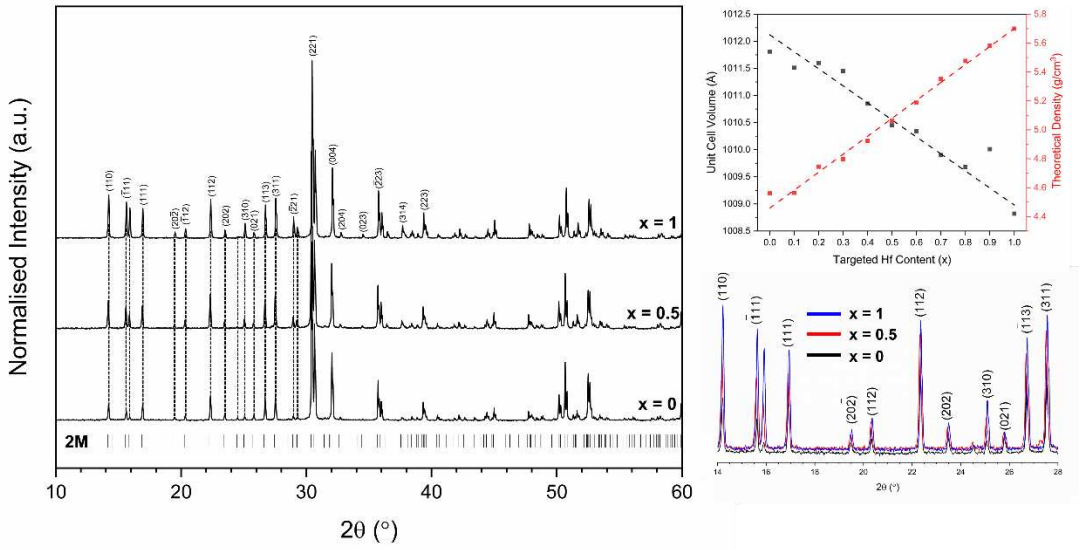

Fig. 1) Powder X-ray diffraction data for x = 0, 0.50 and 1.00 showing the allowed reflections for the zirconolite-2M structure and (hkl) values for selected reflections in the low 2θ range. Insets show **(1)** magnified reflections in the range 14° ≤ 2θ ≤ 28°

and **(2)** unit cell volume (Å^3) and theoretical density (g/cm^3) as a function of targeted Hf^{4+} content, using values calculated from Rietveld analysis of powder diffraction profiles.

A series of 11 zirconolite-hafnolite pellets were produced including both end-member compositions and first analysed by powder X-ray diffraction (**Fig. 1**) and scanning electron microscopy (**Fig. 2**) to establish phase purity and determine substitution limits of HfO_2 within the nominal solid solution $CaZr_{1-x}Hf_xTi_2O_7$. The observed reflections in the powder diffraction profile were all readily indexed to the zirconolite-2M structure and, with the exception of x = 0.70, 0.80 and 0.90, no visible phase separation was observed. An example of the microstructure for x = 0.80 is provided in **Fig. S1** and appears to show small Hf/Ti-rich inclusions, likely of the $HfTiO_4$ structure-type. The $HfTiO_4$ reflections were not readily indexable due to the overlap in 2θ position with the dominant (221) reflection for the 2M structure. Rietveld analysis was performed using a zirconolite-2M (C2/c) structural model, wherein the occupancy of the *Zr1* site was modified to partially include Hf^{4+} fixed according to the target stoichiometry. The unit cell parameters and site occupancy of *Ca1*, *Ti1*, *Ti2* and *Ti3* sites were allowed to simultaneously refine, and the refinements all converged with good statistics (**Table 1**). It was noted that including an additional $HfTiO_4$ phase to the model for x = 0.70 did nothing to further improve the refinement statistics and estimated the relative phase fraction to be < 2 wt. %, hence was not included in any subsequent analysis. The relative intensity of the indexed reflections was observed to increase when data were normalised to the intensity of the dominant (221) reflection (see inset of **Fig. 1**) attributed to an increased scattering factor. As the intensity of scattered X-rays scales with Z, this effect was attributed to the progressive substitution of Hf (Z = 72) for Zr (Z = 40). The unit cell volume was observed to steadily decrease as a function of Hf^{4+} content (see inset of **Fig. 1**) on account of the small variation in ionic radii between Zr^{4+} and Hf^{4+} (0.78 Å and 0.76 Å in 7-fold coordination, respectively). The obtained unit cell dimensions are in good agreement with those previously reported in the literature [3]. The theoretical density of the zirconolite phase was observed to steadily increase with Hf^{4+} content, consistent with the density of Zr and Hf oxides (5.67 and 9.68 g/cm^3, respectively).

Table 1) Unit cell parameters for the zirconolite-2M phase obtained by Rietveld analysis using a 2M (C2/c) structural model.

(x)	a (Å)	b (Å)	c (Å)	β (°)	V (Å^3)	R_{wp}	GOF
0.00	12.4447(2)	7.2728(1)	11.3726(2)	100.5760(12)	1011.81(3)	12.53	2.08
0.10	12.4416(2)	7.2725(1)	11.3723(2)	100.5712(10)	1011.51(3)	11.40	2.02
0.20	12.4451(5)	7.2719(3)	11.3712(5)	100.5820(2)	1011.60(8)	15.11	2.54
0.30	12.4402(2)	7.2725(1)	11.3728(2)	100.5713(11)	1011.45(3)	10.97	2.05
0.40	12.4369(2)	7.2715(1)	11.3704(2)	100.5650(9)	1010.85(3)	9.55	1.95
0.50	12.4358(2)	7.2711(1)	11.3675(2)	100.5633(11)	1010.45(3)	10.01	1.90
0.60	12.4340(2)	7.2714(1)	11.3675(2)	100.5626(10)	1010.34(2)	10.00	2.10
0.70	12.4318(2)	7.2704(1)	11.3660(2)	100.5616(11)	1009.90(3)	9.86	2.10
0.80	12.4311(2)	7.2703(1)	11.3643(2)	100.5595(11)	1009.68(3)	9.91	1.98
0.90	12.4327(2)	7.2717(1)	11.3650(2)	100.5647(13)	1010.01(4)	10.36	1.99

1.00	12.4267(2)	7.2694(1)	11.3599(2)	100.5557(10)	1008.82(2)	9.67	2.05

SEM observations of the polished microstructures highlighted that high density materials were formed throughout the solid solution (**Fig. 2**). Minimal porosity was observed, and this was reflected by the obtained Archimedes and He-pycnometry density measurements, indicating %TD between ~ 93% and ~ 98%. The average bulk composition of each microstructure was obtained by EDS analysis (**Table S1**) which produced average values in good agreement with the targeted composition, with each composition normalised to seven oxygen atoms per formula unit.

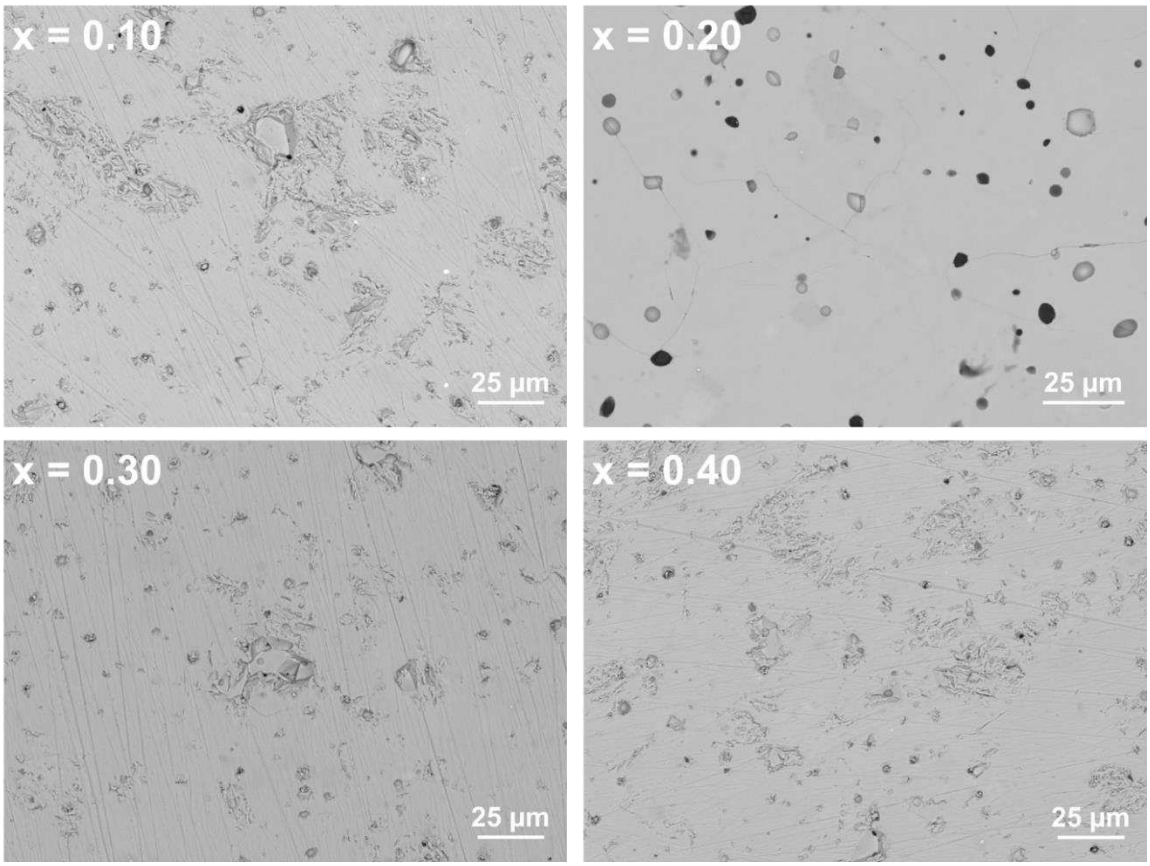

Fig. 2) Backscattered electron micrograph images of polished 0.10 ≤ x ≤ 0.40 compositions detailing single phase zirconolite-2M.

The fits of Hf L_3-edge EXAFS spectra for x = 0.1, 0.5, and 1.0 compositions are shown in **Fig. 3**. The Hf L_3-edge EXAFS was first fitted for the HfO_2 reference sample to determine a suitable amplitude reduction factor ΔE_0 of 1. For x = 1.0 (R-factor = 0.0122) the model utilised a split first O shell with 5 O backscatterers at 2.11 (1) Å and 2 O backscatterers at 2.35 (3) Å , along with 2.5 Ti backscatters (with the 0.5 degeneracy contribution accounting for the 50% statistically occupied Ti site within zirconolite-2M) at 3.28 (1) Å, 2 Ca backscatterers at 3.65 (2) Å, 1 Hf backscatterer at 3.90 (3) Å, and 2 Ca backscatterers at 4.06 (3) Å. For x = 0.5 (R-factor = 0.0164), a very similar best fit model was used, however both Zr and Hf scattering paths were included, each with amplitude reduction factors (S_0^2)

scaled by a factor of 0.5, as degeneracies below 1 are known to produce unstable fits in Artemis. The model included 5 O backscatterers at 2.12 (1) Å, 2 O backscatterers at 2.35 (2) Å, 2.5 Ti backscatterers at 3.25 (2) Å, 2 Ca backscatterers at 3.49 (4) Å, 0.5 Hf backscatterers at 3.70 (3) Å, 0.5 Zr backscatterers at 3.47 (3) Å, and 2 Ca backscatterers at 4.16 (4) Å. For x = 0.1 (R-factor = 0.0115), a narrower Hanning window function was used due to the reduced signal to noise ratio from the Hf L_3-edge (low Hf concentration). This resulted in fewer scattering paths being included to prevent over-parameterising and hence over-constraining the model within the fitted window. While ideally, a similar model would be used between all compositions, this compromise was required to produce an acceptable best fit model. The paths included were 5 O backscatterers at 2.12 (1) Å, 2 O backscatterers at 2.35 (3) Å, and 2.5 Ti backscatterers at 3.27 (1) Å.

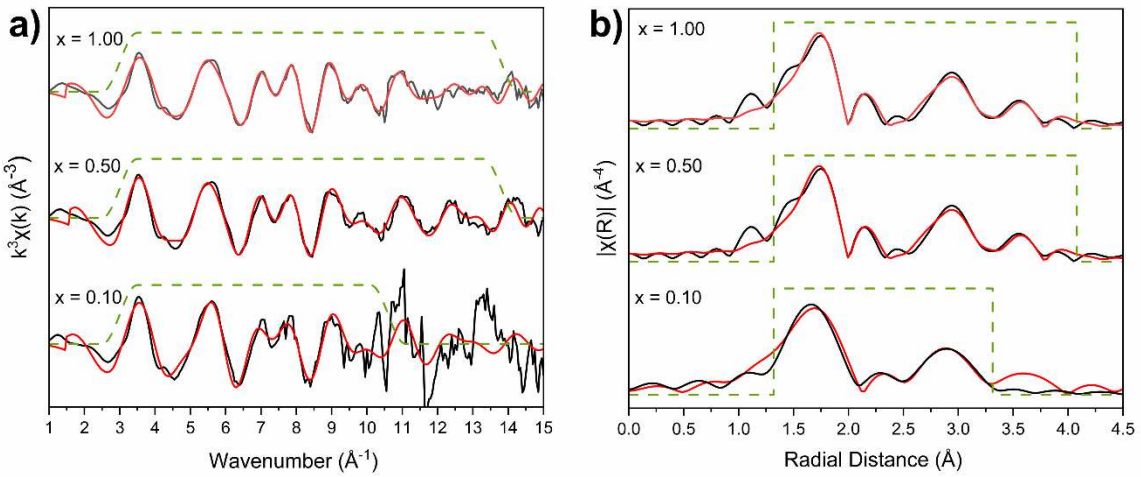

Fig. 3) a. Hf L_3 k^3 weighted EXAFS. **b**. Fourier transform of the k^3-weighted EXAFS. Black lines are data, red lines are best fit models, green dashed lines show the Hanning window function.

Table S2 summarises the parameters used to produce the discussed fits. All three fits use a scattering model that corresponds well to the known structure of zirconolite-2M giving confidence to the outputted atomic positions and resulted in low R-factors (< 0.02) indicating the quality of the fit is strong. For all three compositions the total degeneracy for the first oxygen shell around Hf^{4+} was found to be 7. Bond valance sums (b.v.s.) were calculated for the first oxygen shell of Hf^{4+}, which were found to be acceptably close to 4 v.u. (valance units) for each model, confirming chemical plausibility. First oxygen shell b.v.s. of each model are presented within **Table S2**, also shown are the percentage of variables used for fitting out of the available independent data points within the fitting windows, fits using >70% of available data points risk being over constrained. Overall, the results of these fits support the proposed solid solution mechanism whereby Hf^{4+} largely replaces Zr^{4+} in the 7-fold coordinated oxygen environment, although a small degree of Ti/Zr site mixing is expected in all cases. The radial distance of the oxygen scatters can be seen to increase slightly with Hf content, indicating that the first oxygen shell expands slightly when Zr^{4+} is replaced with Hf^{4+}. Confidence in these results is given by the quality of the fits to the data.

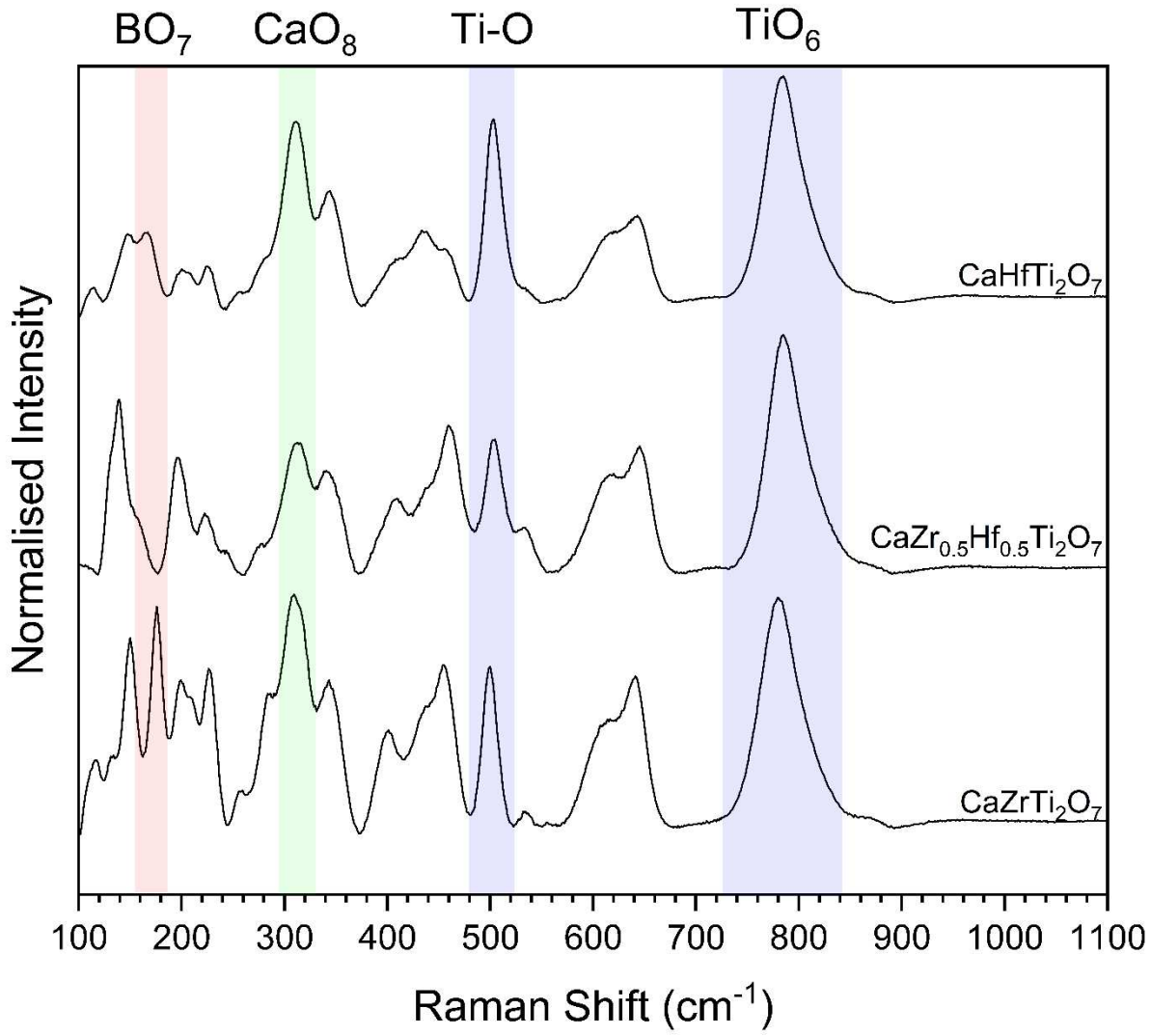

Fig. 4) Raman spectra for $CaZrTi_2O_7$, $CaZr_{0.5}Hf_{0.5}Ti_2O_7$ and $CaHfTi_2O_7$

Raman spectra (**Fig. 4**) showed a series of peaks with endmembers being particularly similar in observed vibrational modes. Whilst the Raman spectra of zirconolite has not been formally assigned, the dominant 780 cm^{-1} peak, consistent with the symmetric stretching of TiO_6 polyhedra, is present across the series alongside the characteristic Ti-O torsional vibration at 500 cm^{-1} [10, 11]. The doublet of peaks at 615 cm^{-1} and 640 cm^{-1} are also present across all samples and are typical of zirconolite-2M Raman spectra [12, 13]. The peaks centred around 314 cm^{-1}, which is associated with the CaO_8 polyhedral vibrations, specifically those in the 250 – 380 cm^{-1} remain largely unchanged except for subtle broadening which can be attributed to the poorer sinterability of HfO_2 [11]. The most significant changes in the Raman spectra are within the 100 – 240 cm^{-1} region, with the 179 cm^{-1} peak at the Zr endmember, typically associated with ZrO_7 vibration (or more generally BO_7 when considering the ABC_2O_7 general structure) red-shifting to 165 cm^{-1} with Hf. This indicates a lower frequency vibration, likely due to the larger atomic mass of the Hf ion. These data indicate a complete substitution of Zr for Hf whilst retaining the monoclinic 2M polytype of zirconolite and confidently demonstrate the dependency of the 179 cm^{-1} spectral line to the intrinsic vibration of ZrO_7 polyhedra.

The thermal properties of a ceramic wasteform govern how the material dissipates radiogenic decay heat from the decay of isotopes such as ^{239}Pu, and could therefore have an effect on material performance. An increased understanding of the thermal and mechanical properties, and such a dependence on composition, is necessary to predict the evolution of key wasteform properties in the disposal environment. This can be further influenced by factors such as the loading, design and geometry of waste packages. The thermal conductivity and diffusivity and specific heat capacity of samples corresponding to x = 0, 0.5 and 1 (i.e. $CaZrTi_2O_7$, $CaZr_{0.50}Hf_{0.50}Ti_2O_7$ and $CaHfTi_2O_7$) were measured by the Laser Flash method (**Fig. 5**). Both the thermal diffusivity (α) and conductivity (*k*) were observed to increase with elevated Hf^{4+} content (**Table 2**) although there is not entirely a clear compositional trend. A literature survey identified limited comparable data sets for the diffusivity and conductivity values for stoichiometric zirconolite and related phases, these are summarised in **Table 2**. Buykx [14] reported both thermal diffusivity (23 °C to 650 °C) and thermal conductivity (23 °C to 475 °C) for $CaZrTi_2O_7$ using the LFA method. The reported thermal conductivity and diffusivity values are both higher across the temperature range than those observed in the present work. Additionally, thermal conductivity was shown to increase slightly with temperature, a trend not observed here. Yin et al. [15] reported thermal conductivities measured by LFA at 25 °C for $Ca_{1-x}Zr_{1-x}Nd_{2x}Ti_2O_7$ ($0 \leq x \leq 0.3$), which ranged between 1.51 to 1.67 W/mK, with no apparent compositional trend. **Table 3** compiles the specific heat capacity (C_p) values for zirconolite systems reported in the literature, along with the results of the present work. Variations in LFA methodology may have contributed to the inconsistencies observed both within the existing literature, and in comparison, with the results of this study. The LFA method for insulating materials is sensitive to both the sample's dimension-to-thickness ratio, and coating procedure which is difficult to normalise. Moreover, the presence of the $(Hf/Ti)O_4$ impurity phase in the x = 1 sample will likely impact a true measurement of conductivity/diffusivity, potentially due to variations in heat capacity and thermal expansion coefficients. Further work will seek to corroborate the influence of both composition and grain size on the thermal properties of zirconolite pellets, including those doped with realistic quantities of Pu surrogates.

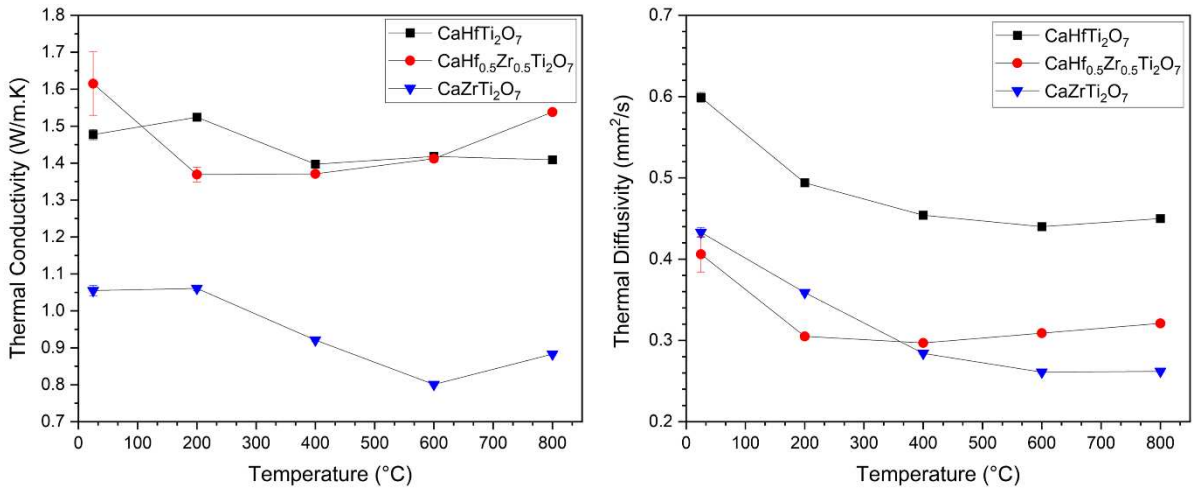

Fig. 5) Measured thermal diffusivity and conductivity for x = 0, 0.50 and 1.00 ceramics in the $CaZr_{1-x}Hf_xTi_2O_7$ system

Table 2) Thermal diffusivity and conductivity values for zirconolite materials identified in the wider literature

Composition	Thermal Diffusivity (mm^2/s)	Thermal Conductivity (W/mK)	Temperature (°C)	Ref.
$CaZrTi_2O_7$	0.43 ± 0.01	1.06 ± 0.01	25	Present work
	0.36 ± 0.01	1.06 ± 0.01	200	
	0.28 ± 0.01	0.92 ± 0.01	400	
	0.26 ± 0.01	0.80 ± 0.01	600	
	0.26 ± 0.01	0.89 ± 0.01	800	
$CaZr_{0.5}Hf_{0.5}Ti_2O7$	0.41 ± 0.02	1.62 ± 0.09	25	Present work
	0.31 ± 0.01	1.37 ± 0.02	200	
	0.30 ± 0.01	1.37 ± 0.01	400	
	0.31 ± 0.01	1.41 ± 0.01	600	
	0.32 ± 0.01	1.54 ± 0.01	800	
$CaHfTi_2O_7$	0.60 ± 0.01	1.48 ± 0.01	25	Present work
	0.50 ± 0.01	1.52 ± 0.01	200	
	0.45 ± 0.01	1.40 ± 0.01	400	
	0.44 ± 0.01	1.42 ± 0.01	600	
	0.45 ± 0.01	1.41 ± 0.01	800	
$CaZrTi_2O_7$	0.88 (0.044)	2.11 (0.25)	23	**[14]**
	0.83 (0.037)	2.31 (0.28)	160	
	0.79 (0.040)	2.34 (0.28)	305	
	0.79 (0.040)	2.42 (0.29)	475	
	0.85 (0.043)	-	650	
$CaZrTi_2O_7$	-	1.57	25	**[15]**
$Ca_{0.95}Zr_{0.95}Nd_{0.1}Ti_2O_7$		1.50		
$Ca_{0.90}Zr_{0.90}Nd_{0.2}Ti_2O_7$		1.67		
$Ca_{0.85}Zr_{0.85}Nd_{0.3}Ti_2O_7$		1.52		
$Ca_{0.80}Zr_{0.80}Nd_{0.4}Ti_2O_7$		1.52		
$Ca_{0.70}Zr_{0.70}Nd_{0.6}Ti_2O_7$		1.66		

Table 3) Specific heat capacity values for zirconolite and related Hf-solid solutions reported in the wider literature

Composition	Method	C_p (J / kg·K)	Temperature (°C)	Ref.
$CaZrTi_2O_7$	LFA	0.593	25	Present work
$CaZr_{0.5}Hf_{0.5}Ti_2O_7$	LFA	0.809	25	Present work
$CaHfTi_2O_7$ + < 2wt% Hf/Ti Rich Impurities	LFA	0.448	25	Present work
$CaZrTi_2O_7$	LFA	0.55	21.85 (295 K)	**[14]**
$CaZrTi_2O_7$ + Excess ZrO2	Adiabatic Calorimetry	0.62	25	**[16]**
$CaZrTi_2O_7$	Adiabatic Calorimetry	0.62	25	**[17]**
$CaZr_{0.26}Hf_{0.74}Ti_2O_7$	Adiabatic Calorimetry	0.51	25	**[18]**
$CaHfTi_2O_7$	Adiabatic Calorimetry	0.49	25	**[18]**
$CaZrTi_2O_7$	GULP Potenital Models	0.55	21.85 (295 K)	**[19]**
$CaZrTi_2O_7$	Drop Calorimetry	0.62	25	**[20]**
$CaZrTi_2O_7$	Drop Calorimetry	0.67	25	**[21]**

4 Conclusions

The UK separated Pu inventory could potentially be managed by a strategy of immobilisation proceeded by permanent geological disposal. The NDA seeks to further its understanding of the thermal and structural properties of potential ceramic wasteforms, for which zirconolite ($CaZrTi_2O_7$) is a candidate, inclusive of a further underpinning of the substitution behaviour of potential neutron absorbing additives within the zirconolite structure. This also constitutes a requirement to understand the isolated effects of cation substitution within specific lattice sites. To this end, the $CaZr_{1-x}Hf_xTi_2O_7$ system was fabricated and demonstrated complete solid solubility of Hf^{4+} at low-to-moderate concentration ($x \leq 0.60$) confirmed by powder X-ray diffraction, electron microscopy and Raman spectroscopy. Our data provide underpinning evidence that Hf^{4+} successfully substitutes for Zr^{4+} in the zirconolite structure, without promoting polytype transformations or (at low to moderate concentrations) resulting in phase segregation. Rietveld analysis of the diffraction data was consistent with Hf^{4+} occupying Zr^{4+} sites within the zirconolite structure. Complementary Hf L_3-edge EXAFS fitting of Hf-substituted zirconolite (reported within for the first time) were consistent with this substitution mechanism. The thermal diffusivity and conductivity were also observed to vary with Hf^{4+} content yet no clear compositional trends were identified, highlighting the requirement for further systematic study in this area using a larger data set with more granular compositional intervals. These data contribute to a more holistic understanding of the zirconolite system and will further inform potential solid solution regimes for materials containing Pu and neutron absorbing additives. Further work will seek to understand the thermal and structural

properties in wasteforms containing a realistic Pu surrogate fraction, with a view to better inform disposability.

5 Acknowledgements

This research utilised the HADES/MIDAS facility at the University of Sheffield established with financial support from EPSRC and BEIS, under grant EP/T011424/1 [22]. Lewis Blackburn gratefully acknowledges the Royal Academy of Engineering for support through the Research Fellowship scheme. We wish to acknowledge the Henry Royce Institute for Advanced Materials, funded through EPSRC grants EP/R00661X/1, EP/S019367/1, EP/P02470X/1, EP/P025285/1 and EP/X52850X/1, for the financial support and Netzsch LFA 467 Hyper Flash access at The University of Sheffield. Access to Diamond Light Source Beamline B18 is gratefully acknowledged under Proposal SPENND SP37736. We are grateful to EPSRC for funding studentships through the SATURN (EP/S022295/1) and GREEN (EP/Y034856/1) Centres for Doctoral Training.

6 Author contributions

AM: Formal analysis, investigation, data curation, original draft preparation. AAF: Formal analysis, investigation, data curation. LTH: Formal analysis, investigation, data curation. MM: Formal analysis, investigation, data curation. IA: Formal analysis, investigation, data curation. AHR: Formal analysis, investigation, data curation. MCS: IA: Formal analysis, investigation, data curation. LRB: Conceptualisation, investigation, resources, supervision, project administration, funding acquisition.

7 Data Availability

The data to support the findings of this study are available from the corresponding author upon reasonable request.

8 Declarations

Conflict of interest: The authors declare no known conflicts of interest.

9 References

[1] Bodel, W., Bull, A., Butler, G., Harrison, R., Matthews, J., Warrilow-Brennan, D., & Sharrad, C. Managing the UK plutonium stockpile: no easy choices (2023).

[2] Nuclear Decommissioning Authority (NDA). Progress on Plutonium Consolidation, Storage and Disposition (2019).

[3] Blackburn, L.R.; Corkhill, C.L.; Hyatt, N.C. A Review of Zirconolite Solid Solution Regimes for Plutonium and Candidate Neutron Absorbing Additives. *Ceramics*, 6, pp. 1330-1347 (2023).

[4] Vance, E.R., Jostsons, A., Day, R.A., Ball, C.J., Begg, B.D., Angel, P.J. Excess Pu Disposition in Zirconolite-Rich SYNROC. *Mat. Res. Soc. Symp. Proc*. Vol. 412 (1996).

[5] Putnam, R.L., Navrotsky, A., Woodfield, B.F., Shapiro, J.L., Stevens, R.B., Boerio-Goates, J. Thermochemistry of Hf-Zirconolite, $CaHfTi_2O_7$. *Mat. Res. Soc. Symp. Proc*. Vol. 556 (1999).

[6] Begg, B.D., Vance, E.R., Day, R.A., Hambley, M., Conradson, S.D. Plutonium and Neptunium Incorporation in Zirconolite. *Mat. Res. Soc. Symp. Proc*. Vol. 465 (1997).

[7] Zhang, K., Yin, D., He, Z., Luo, B., Zhang, H. Combustion synthesis of Hf-doped zirconolite-rich composite waste forms and the aqueous durability. *Journal of Advanced Ceramics*, 8(3), pp. 448-455 (2019).

[8] Caurant, D., Loiseau, P., Bardez, I. Structural characterisation of Nd-doped Hf-zirconolite $Ca_{1-x}Nd_xHfTi_{2-x}Al_xO_7$ ceramics. *Journal of Nuclear Materials*, 407, pp. 88-89 (2010).

[9] Caurant, D., Loiseau, P., Bardez, I., Gervais, C. Effect of Al2O3 concentration on zirconolite ($Ca(Zr,Hf)Ti_2O_7$) crystallization in (TiO_2,ZrO_2,HfO_2)-rich SiO_2–Al_2O_3–CaO–Na_2O glasses. *Journal of Materials Science*, 42, pp. 8558-8570 (2007).

[10] Salamat, A., McMillan, P. F., Firth, S., Woodland, K., Hector, A. L., Garbarino, G., Stennett, M. C., Hyatt, N. C. Structural Transformations and Disordering in Zirconolite ($CaZrTi_2O_7$) at High Pressure, *Inorg. Chem*. 52, pp. 1550–1558 (2013).

[11] Song, Y., Ji, X., Tang, K., Zhang, Y., Xu, T., Ji, S., Duan, T. The structural evolution and chemical durability of the $CaZr_{1-x}Sm_xTi_{2-x}Nb_xO_7$ defect fluorite-derived ceramics, *J. Am. Ceram. Soc*., 108, e20693 (2025).

[12] Jafar, M., Achary, S. N., Salke, N. P., Sahu, A. K., Rao, R., Tyagi, A. K. X-ray diffraction and Raman spectroscopic investigations on $CaZrTi_2O_7$-$Y_2Ti_2O_7$ system: Delineation of phase fields consisting of potential ceramic host materials, *J. Nucl. Mater.*, 475, pp. 192–199 (2016).

[13] Blackburn, L. R., Townsend, L. T., Lawson, S. M., Mason, A. R., Stennett, M. C., Sun, S. K., Gardner, L. J., Maddrell, E. R., Corkhill, C. L., Hyatt, N. C. Phase Evolution in the $CaZrTi_2O_7$ – $Dy_2Ti_2O_7$ System: A Potential Host Phase for Minor Actinide Immobilization, *Inorg. Chem*. 61, pp. 5744–5756 (2022).

[14] Buykx, W. J. Specific heat, thermal diffusivity and thermal conductivity of synroc, perovskite, zirconolite and barium hollandite. J*. Nucl. Mater*., vol. 107, no. 1, pp. 78–82 (1982).

[15] Yin, D., Zhang, K., Peng, L., He, Z., Lui, H., Zhang, H., Lu, X. Solid-state reaction synthesis and chemical durability studies in Nd-doped zirconolite-rich ceramics. *Journal of Rare Earths*, vol. 36, 5, pp. 492-498 (2018).

[16] Woodfield, B. F., Boerio-Goates, J., Shapiro, J. L., Putnam, R. L., Navrotsky, A. Molar heat capacity and thermodynamic functions of zirconolite $CaZrTi_2O_7$, *J. Chem. Thermodyn*., vol. 31, no. 2, pp. 245–253, (1999).

[17] Putnam, R. L., Navrotsky, A., Woodfield, B. F., Boerio-Goates, J., Shapiro, J. L. Thermodynamics of formation for zirconolite ($CaZrTi_2O_7$) from T = 298.15 K to T = 1500 K. *J. Chem. Thermodyn*., vol. 31, no. 2, pp. 229–243 (1999).

[18] Stevens, R., Hom, B. K., Boerio-Goates, J., Woodfield, B. F., Putnam, R. L., Gutierriez, J., Navrotsky, A. Molar heat capacities and thermodynamic functions of $CaHfTi_2O_7$(cr) and $CaZr_{0.26}Hf_{0.74}Ti_2O_7$(cr). *J. Chem. Thermodynamics*, 33, pp. 1441-1455 (2001).

[19] Veiller, L., Crocombette, J. P., Ghaleb, D. Molecular dynamics simulation of the α-recoil nucleus displacement cascade in zirconolite. *J. Nucl. Mater*., vol 306, 1, pp. 61-72 (2002).

[20] Pöml, P., Geisler, T., Konings, R. J. M. High-temperature heat capacity of zirconolite ($CaZrTi_2O_7$). *J. Chem. Thermodynamics*, 38, 8, pp. 1013-1016 (2006).

[21] Jafar, M., Phapale, S., Achary, S. N., Mishra, R., Tyagi, A. K. High-temperature crystallographic and thermodynamic investigations on synthetic zirconolite ($CaZrTi_2O_7$). *J. Therm. Anal. Calorim*., vol. 131, no. 3, pp. 2709–2718 (2018).

[22] Hyatt, N. C., Corkhill, C. L., Stennett, M. C., Hand, R. J., Gardner, L. J., Thorpe. C. L. The HADES facility for high activity decommissioning engineering & science: part of the UK national nuclear user facility. *IOP Conf. Ser. Mater. Sci. Eng*., 818, Article 012022 (2020).